Modelling Size of Inclusions in Air Entrainment Models for Eulerian RANS Simulations

Federico Baraglia, Jérôme Laviéville, Nicolas Mérigoux and Olivier Simonin

November 3, 2023

MODELING SIZE OF INCLUSIONS IN AIR ENTRAINMENT MODELS FOR EULERIAN RANS SIMULATIONS

Federico, Baraglia[1], Jérôme, Laviéville, Nicolas, Mérigoux
Mécanique des Fluides, Energie, Environnement, EDF R&D, 6 Quai Watier Chatou 78400 FRANCE
federico.baraglia@edf.fr

Olivier, Simonin
Institut de Mécanique des Fluides de Toulouse, Université de Toulouse, CNRS, INPT, UPS, 2 All. du professeur Camille Soula Toulouse 31400 FRANCE

KEY WORDS

Computational fluid dynamics, Multiphase flows, turbulence, bubbly flow

ABSTRACT

In this paper, we present a new air entrainment model which predicts the bubble diameter for entrained air based on Hinze theory. In this theory, after bdubbles are created at the free-surface, they are successively broken down into smaller and smaller structures due to turbulent breakup. When turbulence is no longer intense enough, the bubble diameter stabilises. By assuming this turbulent breakup occurs close to the free surface and rapidly compared with other flow characteristics, it is possible to determine the diameter of stable bubbles when they are entrained below the free-surface. This model is implemented in a multifluid RANS solver with an interfacial area transport equation to account for bubble diameter polydispersion. The diameter calculated from Hinze theory determines how the interfacial area transport equation must be adapted to account for air entrainment in the simulations.

Air entrainment is first generally described before introducing the model which is developed in neptune_cfd, a finite volume RANS solver developed by EDF, CEA, IRSN and Framatome which allows for the numerical resolution of separate Reynolds averaged Eulerian equations (mass, momentum and energy) for n phases coupled by interfacial transfer terms. Results obtained are then compared with experimental data in several cases representative of air entrainment phenomena. A special focus is made on mesh convergence and on the model relation with the mesh.

1. INTRODUCTION

Air entrainment or air aeration in air-water flows is defined as the transition that occurs when continuous air present on top of water is transported, in the forms of bubbles or pockets, below the free surface of a liquid. This phenomenon is present in natural flows: breaking waves, hydraulic jumps or highly turbulent free-surface flows [1, 2]. However, it can also appear in industrial facilities like water jets impacting free-surface flows. In natural fl[1]ows, air aeration can change the transfer properties between the liquid and the gas which can in turn change the chemical and physical properties under water. Understanding aeration of water flows represent a key challenge to measure the impact it can have on wildlife. In industrial processes, air aeration can enhance the speed of chemical reactions or change particles transportation behaviour inside the liquid. In waste processing plants for example, it is a phenomenon highly sought after since it can speed up the treatment.

Aeration in air-water flows - or liquid-gas flows more generally - can occur in different scenarios [3] [4]. In some specific cases it results from the geometric entrapment of air around water. In other cases, air is entrained due to to the interaction between a water turbulent vortex and the free surface [5]. In the case of a breaking wave, the air pocket geometrically entrapped around water is then subsequently divided into smaller and smaller pockets by turbulent water eddies until only small bubbles remain. The interaction between eddies and the free surface tend to generate bubbles with different diameters depending on the

---

[1] Corresponding author

intensity of the collision, the characteristics of the eddy and the state of the free-surface flow. It also depends on the physical characteristics of the fluids. All in all, the two variables describing this phenomenon are the mass transfer rate from the continuous air above the free-surface to the dispersed inclusions below the free-surface and the size distribution of bubbles created by this process.

There are numerous experimental setups which aim at understanding and characterising the phenomenon of air entrainment in different scenarios. These scenarios include breaking waves, impacting jets or hydraulic jumps. In all of them, the main difficulties lie within characterising the bubbles created during the entrainment process. Unfortunately, the size distribution of bubbles below the free-surface represents the most important unknown when designing a model for air entrainment. Even in simple cases such as thin impacting jets, the large amount of bubble created makes it difficult to accurately define the bubble plume. 3D imaging techniques have been used [6], but this technique requires a lot of material and heavy post-processing methods. The other widely spread technique consists in the use of probes. These sensors rely on the different physical characteristics of the fluids to determine the frequency of phase change at the position of the probe. Usually, probes rely on conductivity measurements or optical properties measurements. With the frequency of phase change, by assuming the inclusions are spherical, it is possible to measure its size. Compared with the first technique, the second one suffers from a lack of consistency when the hypothesis of spherical inclusion is not applicable. Also, the presence of the probe may alter the inclusions thus making the technique slightly less accurate. With air entrainment characterisation, some experiments have also tried correlating jet roughness properties with bubble plume statistics [7].

From a simulation point of view, modeling air entrainment remains a challenge in most of the techniques used in computational fluid dynamics. In volume of fluid (VOF), smooth particle hydrodynamics (SPH) or multi-fluid simulations, the process of air entrainment is not natural and needs to be taken into account through modeling. Direct numerical simulations with volume of fluid methods may be the only simulation technique where air entrainment does not have to be modelled. However, due to the size of entrained bubbles, it is still considered to be a challenging endeavour [8] [9]. The goal of an entrainment model is to predict two variables: the quantity of air entrained and its size distribution. The first variable has been studied extensively and many models have been developed based either on mechanistic methodologies [10] [11] [12] [13] or experimental correlations [14]. On the other hand, the size distribution of entrained air is not commonly studied, and, in many cases, experimental results are needed to determine it. In the GENTOP model [11], air is decomposed into two fields, a dispersed and a continuous one. In the dispersed field, different sizes are accounted through a population balance method and mass transfer occur between the different group of the population due to coalescence and breakup. Air entrainment is modelled through a transfer from the continuous air field to the groups of the dispersed air field. If the total mass transfer follows an air entrainment model, the choice of the group the mass is transferred to heavily relies on experimental validation. Similarly, in the work from [15] and [16], gas is transferred to the dispersed bubble field through an explicit source term. However, no details are given for the bubble size distribution.

The main goal of this paper is to present a model for the size distribution of air bubbles entrained below the free-surface based on the Hinze scale. In the following paragraphs, we only consider an air-water mixture but the concepts can be generalised to any two-fluid flows. We start by presenting the CFD framework before introducing the new model for bubble size distribution and how it is embedded in the framework. Then, the model is compared against experimental data for three different cases where air entrainment is supposed to be caused by different phenomenon.

2. N-EULER RANS MODELING

All simulations presented in this paper are performed with neptune_cfd, an in-house 3D RANS solver generalizing to n phases the two fluids formulation [17]. This code solves conservation equations for mass, momentum and energy for each phase assuming they are coupled through interfacial transfer terms and that there is only one pressure. The resolution is performed with a finite volume scheme and collocated variables and is compatible with full-unstructured mesh, however, in this paper, we only perform computations on Cartesian meshes. Additional conservation equations are introduced for the turbulent quantities. First and second order models such as k-ϵ or R_{ij}-ϵ SSG formulations. When solved, these equations give access to ϵ_w

the water turbulent kinetic energy dissipation used in the air entrainment model. By design, the method associates one set of fields (volume fraction, velocity, turbulent quantities) to every phase. Then, depending on the local flow characteristics, large interfaces can be identified through a process described in [18]. In those regions, interfacial transfer terms are modified to match free-surface modeling techniques. In all other regions, dispersed models are applied. In order to ensure numerical stability, a smooth transition is imposed between both approaches. This allows for numerical simulation of multiphase flows where multiple regimes can be encountered. Figure 1 shows a typical domain segmentation where different regimes are found. Finally, in regions containing dispersed inclusions, diameter polydispersion is considered through an interfacial area transport equation.

2.1 Governing equations

Throughout the paper, the flows are assumed incompressible, isothermal and without phase change, only mass and momentum balance equations are relevant. The fluids mass and momentum conservation equations are obtained following the methodology described in [17]. The local instantaneous equations and the jump conditions at the interface are derived and phase averaged. Assuming the interface separating two phases is infinitely thin and massless, with f representing a fluid phase, α_f and ρ_f its mean volume fraction and mass per unit volume, the equations reduce to:

$$\frac{\partial}{\partial t}\left(\alpha_f \rho_f\right) + \frac{\partial}{\partial x_i}\left(\alpha_f \rho_f U_{f,i}\right) = 0 \tag{1}$$

$$\frac{\partial}{\partial t}\left(\alpha_f\, \rho_f\, U_{f,i}\right) + \frac{\partial}{\partial x_j}\left(\alpha_f\, \rho_f\, U_{f,i} U_{f,j}\right) = \alpha_f\, \rho_f\, g_i\, - \frac{\partial}{\partial x_j}\left\langle \rho\, u''_{f,i} u''_{f,i} \chi_f \right\rangle + \frac{\partial}{\partial x_j}\left(\alpha_f\, \Sigma_{f,ij}\right) + \sum_{g\neq f} I_{g\to f,i} \tag{2}$$

Where $\boldsymbol{u_f} = \boldsymbol{U_f} + \boldsymbol{u_f}'$ is the Reynolds decomposition of the fluid velocity, $\boldsymbol{g}$ is gravity, χ_f is the indicator function of phase f, $\Sigma_{f,ij}$ is the mean fluid stress tensor and $\boldsymbol{I_{g\to f}}$ is the mean momentum transfer from phase g to phase f. Since we are considering Newtonian fluids, the mean fluid stress tensor can be written:

$$\Sigma_{f,ij} = -P\delta_{ij} + T_{f,ij} \tag{3}$$

Where P is the unique mean pressure and $T_{f,ij}$ is the dissipative part of the stress tensor. The mean momentum conservation equation can therefore be written as follows:

$$\frac{\partial}{\partial t}\left(\alpha_f \rho_f U_{f,i}\right) + \frac{\partial}{\partial x_j}\left(\alpha_f \rho_f U_{f,i} U_{f,j}\right) = \alpha_f \rho_f g_i - \frac{\partial}{\partial x_j}\left\langle \rho u''_{f,i} u''_{f,j} \chi_f \right\rangle - \alpha_f \frac{\partial P}{\partial x_i} + \frac{\partial}{\partial x_j}\left(\alpha_f T_{f,ij}\right) + \sum_{g\neq f} I'_{g\to f,i} \tag{4}$$

Where $\mathrm{I}'_{g\to f,i} = \mathrm{I}_{\boldsymbol{g\to f,i}} - \mathrm{P}\frac{\partial \alpha_\mathrm{f}}{\partial \mathrm{x\_i}}$ is the mean momentum transfer from phase g to phase f reduced by the mean pressure gradient contribution. We neglect the surface tension and, additionally, the phases are supposed to partition the total domain.

$$I_{g\to f,i} + I_{f\to g,i} = 0 \tag{5}$$

$$\sum_f \alpha_f = 1 \tag{6}$$

For dispersed inclusions, governing equations are obtained from a probability density function and stochastic modeling framework [19]. These are different from the conservation equations derived above by nature [20]. However, by rewriting the interfacial transfer terms and assuming the flow is dilute, the equations can be made to match those obtained in continuous flow modeling. Those can be used independently of the flow morphology. In the following section, we consider a new notation: cl and cg represent the continuous liquid and gas volume fraction whereas dl and dg represent the dispersed liquid and gas volume fraction. These do not reflect a distinction in the method since there is only one field per fluid but rather help defining the differences between the large interface interfacial transfer and the dispersed inclusion interfacial transfer.

2.2 Interfacial transfer modeling

As introduced above, in neptune_cfd, each phase can be continuous, dispersed or both depending on the flow characteristics. Large interfaces are identified according to [18] and in every other regions dispersed models are applied. The dispersed model includes a laminar contribution decomposed into drag, shear-induced lift and added-mass. It also includes a turbulent contribution not presented here, more details can be found in [21].

$$\boldsymbol{I'_{cl-dg}} = -\alpha_{cl}\rho_{cl}F_D^{cl-dg}\boldsymbol{V_r^{cl-dg}} - \alpha_{dg}\rho_{cl}C_A^{cl-dg}\frac{d\boldsymbol{V_r^{cl-dg}}}{dt} - \alpha_{dg}\rho_{cl}L^{cl-dg}\left(\boldsymbol{U_{dg}} - \boldsymbol{U_{cl}}\right) \wedge (\nabla \times \boldsymbol{U_{cl}}) \tag{7}$$

Where F_D^{cl-dg} is the drag coefficient between phase cl and dg, $\boldsymbol{V}_{\boldsymbol{r}}^{\boldsymbol{cl-dg}} = \boldsymbol{U}_{\boldsymbol{dg}} - \boldsymbol{U}_{\boldsymbol{cl}}$ is the average relative velocity, C_A^{cl-dg} is the added-mass coefficient and L^{cl-dg} is the lift coefficient. The drag coefficient for bubbles is based on empirical correlations established by [22], details on the lift coefficient can be found in [23] and the expression for the added-mass coefficient in [24]. In cells containing a free-surface of normal $\boldsymbol{n}$, the interfacial transfer term contains a normal contribution which numerically enforces the condition $\left(\boldsymbol{U}_{\boldsymbol{cl}} - \boldsymbol{U}_{\boldsymbol{cg}}\right).\boldsymbol{n} = 0$ and an anisotropic friction term.

$$I'_{cl\rightarrow cg,i} = \alpha_{cg}\alpha_{cl}\left(\alpha_{cl}\rho_l + \alpha_{cg}\rho_g\right)\frac{C_\tau}{\Delta t}\left[\left(\boldsymbol{u}_{\boldsymbol{cl}} - \boldsymbol{u}_{\boldsymbol{cg}}\right).\boldsymbol{n}\right].\boldsymbol{n} - \rho_l u_{cg}^* A_i \frac{\boldsymbol{u}_{\boldsymbol{cl}} - \boldsymbol{u}_{\boldsymbol{cg}}}{\left|\boldsymbol{u}_{\boldsymbol{cl}} - \boldsymbol{u}_{\boldsymbol{cg}}\right|} \qquad (8)$$

Where C_τ is an empirical parameter, Δt is the numerical time step, A_i is the free-surface area and u_{cg}^* is the friction velocity. Cells flagged as containing a large interface (LI) and adjacent cells in the normal direction to the interface can be used to determine friction velocities. This requires the use of methods like those applied in boundary layer theory. Sub-grid free-surface roughness is also included in the process. More details on the algorithm can be found in the original paper [18]. Turbulence models are modified near the free-surface, the details can be found in [25].

In order to ensure consistency, the transition between large interfaces and dispersed models is performed smoothly [26]. A weighting coefficient γ ensures the transition between the two methods via:

$$\boldsymbol{I}'_{\boldsymbol{cl\rightarrow g}} = \gamma \boldsymbol{I}'_{\boldsymbol{cl\rightarrow dg}} + (1-\gamma)\boldsymbol{I}'_{\boldsymbol{cl\rightarrow cg}} \qquad (9)$$

Where,

$$\gamma = \beta\left(1 - \min(f_c, 1)\right) \qquad (10)$$

and β is a continuous function which values 0 when $\alpha_l = 0$ and 1 when $\alpha_l = 1$ and f_c depends on the local flow characteristics. Figure 1 sums up the different zones in which the models are relevant in neptune_cfd.

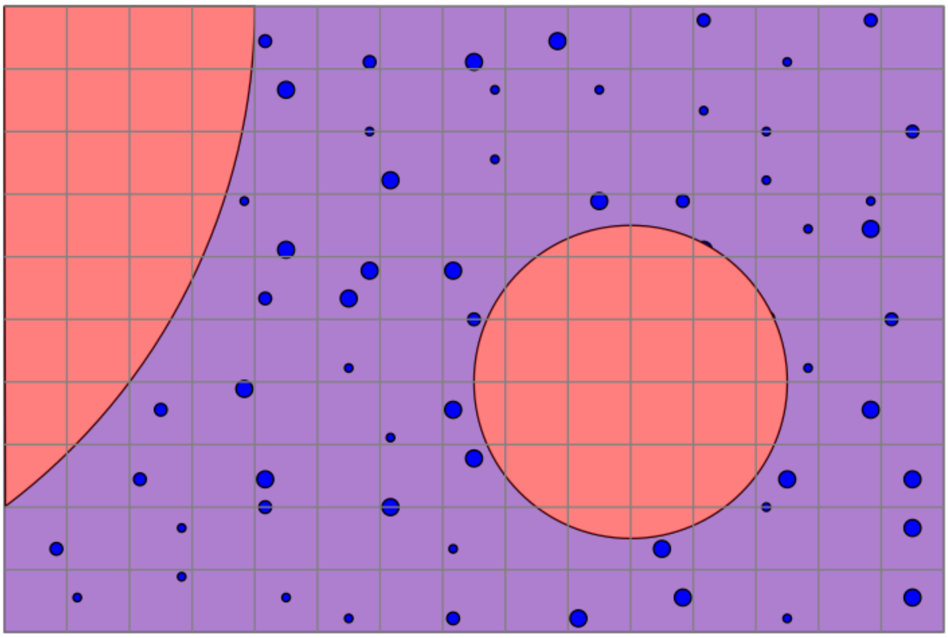

Figure 1: Sketch showing the different models applied in different regions of the domain depending on the flow characteristics. The red zones are continuous structures, their interface with the purple region is treated with the large interface model. The blue regions are small inclusions treated with the dispersed model. The two techniques combined constitute the generalized large interface model from neptune_cfd.

2.3 Interfacial area modeling

In the previous section, interfacial transfer terms have been presented. Their value, in the dispersed case, is closely related to the value of the interfacial area a_i, the amount of interfacial surface area per unit volume. By definition, an interfacial area is associated to all phases. In neptune_cfd, it is possible to perform simulations with a constant or varying diameter. We will focus exclusively on the case where inclusions diameters vary. The following presentation is a short summary of the method developed and presented in

[27]. For more details on the matter, readers are invited to refer to the original publication. The method consists in describing the set of dispersed inclusions with a probability density function (PDF) F, to express the evolution equation for this equation and then to introduce the statistical moments of the PDF. When a particle diameter is included as a variable of the phase space, interfacial area and volume fraction of dispersed inclusions can be regarded as moments of the PDF. Evolution equations for those are then derived and mathematically closed assuming there are no phase change and that dispersed inclusions are incompressible.

$$\frac{\partial a_i}{\partial t} + \nabla.\left(a_i \langle \boldsymbol{w} \rangle_{d^2}\right) = \int \dot{F_{c,b}} \pi d^2 \partial d \partial \boldsymbol{w} \qquad (11)$$

Where a_i is the interfacial area, $\boldsymbol{w}$ is the bubble velocity, $\langle \mathbf{w} \rangle_{d^2}$ is the mean bubble velocity average weighted by d^2 and $\dot{F}_{c,b}$ is the variation of F due exclusively to coalescence and breakup events. Their expression is described in details in [27] and is inspired from coalescence and breakup models found in [28].

$$\langle \boldsymbol{w} \rangle_{d^2} = \frac{\int F w d^2 \partial d \partial w}{\int F d^2 \partial d \partial w} \qquad (12)$$

Finally, by assuming a presumed form for the size PDF, it is possible to link the interfacial area and mean volume fraction to the equivalent bubble diameter which is used in the interfacial transfer terms in the momentum balance equation.

3. MODELING AIR ENTRAINMENT

The aim of the current section is to describe how air entrainment can be modelled in the framework of multifluid Eulerian RANS simulations. First, we describe how mass transfer is already accounted by the multifluid model used in neptune_cfd, then we present the hypothesis and modifications which allow the inclusion diameter to be determined. Finally, we review different diameter targets model tested and suggest which one gives the best results.

3.1 Mass transfer from continuous gas to dispersed gas

Within the N-Euler RANS framework of neptune_cfd, there is no need to introduce a supplementary model for mass transfer from continuous air to dispersed air and vice versa. In fact, since only one field is associated to each phase, the mass transfer from continuous to dispersed and from dispersed to continuous is a direct result from the resolution of the mass and momentum coupled balance equations. We recall that, at the beginning of each time-step, a large interface identifying algorithm is used to determine the position of the free-surface. Air mass which is present in water but not included in the large interface is immediately regarded as dispersed bubbles. Tracking the total amount of dispersed or continuous air gives an idea of mass transfer from continuous to disperse.

3.2 modeling entrained inclusions diameter in the interfacial area transport equation framework

As introduced in section 2.3Interfacial area modeling, the simulation output includes the total amount of air transferred between the continuous structures and the dispersed inclusions. This transfer can occur in both directions (air entrainment or detrainment). Since the effects of air detrainment is much more limited, we decide to neglect it. We therefore focus mainly on the transfer from continuous air to dispersed air (air entrainment). When air is transported below the free-surface the interfacial area associated to it tends to be the interfacial area value the mass of entrained air had when it was in a continuous structure. The main issue is that this quantity is arbitrarily set at the beginning of a simulation. This is fine if no air entrainment occurs but as soon as it does, the risk is to introduce a dispersed air mass in the water phase with a completely incorrect diameter. The purpose of the model is to change the interfacial area transport equation to avoid the transfer of arbitrary values when air entrainment occurs. It is divided into two steps, first the interfacial area transport equation is modified to isolate the dispersed phase from the continuous phase and second a source term is added in that equation at the position of the interface to reflect air bubble creation.

If we neglect the coalescence and breakup source terms for the sake of simplicity, express the interfacial area in terms of a variable X such that $\alpha\rho X = a_i$ and use the air mass conservation equation, the interfacial area transport equation reads:

$$\alpha\rho \frac{\partial X}{\partial t} - X\left(\alpha\rho u_{g,i}\right) + \frac{\partial}{\partial x_i}\left(\alpha\rho u_{g,i} X\right) = 0 \qquad (13)$$

The convection term in the last equation is responsible for the transport of interfacial area from the continuous structures to the dispersed inclusions. The main idea is to replace it by a function of the local characteristics in the region identifying the free-surface. Thus, isolating the disperse inclusions from the continuous structures and imposing a diameter for dispersed air created at the free-surface. The new convection term is denoted X_m, unchanged in a region containing dispersed inclusions and accounting air entrainment in a region containing an interface. The transition between the two regions is smoothly performed as it is done for the momentum interfacial transfer terms with the coefficient γ. In cell I, between time steps n and $n+1$, the evolution equation for X is discretised as:

$$\frac{\alpha_I \rho \Omega}{\delta t}\left(X_I^{n+1} - X_I^n\right) - X_I^{n+1} \sum_{J \in V_I} \phi_{IJ} \alpha_{IJ} + \sum_{J \in V_I} \phi_{IJ} \alpha_{IJ} X_{m,IJ}^{n+1} = 0 \qquad (14)$$

Where Ω is the cell volume, V_I are the neighbours of I, ϕ_{IJ} is the mass flux between a neighbouring cell J and cell J, α_{IJ} is defined from the volume fraction in the cells I and J and $X_{m,IJ} = \gamma X_{fs} + (1-\gamma) X_{IJ}$ is the modified value of X in cell I defined from a model X_{fs} which defines the diameter of dispersed air bubbles entrained from the free-surface. Then, by separating the implicit terms from the explicit ones, and by assuming the modification of the convection term is only included in the explicit terms, it is possible to re-organise the terms to match the current form.

$$\left(\frac{\alpha_I \rho \Omega}{\delta t} - \sum_{\phi_{IJ}<0} \phi_{IJ} \alpha_{IJ}\right) X_I^{n+1} = \frac{\alpha_I \rho \Omega}{\delta t} X_I^n - \sum_{\phi_{IJ}>0} \phi_{IJ} \alpha_{IJ} \gamma \left(X_{fs,I}^n - X_I^n\right) - \sum_{\phi_{IJ}<0} \phi_{IJ} \alpha_{IJ} \left(X_{m,J}^n + \delta X_J\right) \qquad (15)$$

Figure 2 shows the two different scenarios encountered and the associated expression of the flux of interfacial area. The red cell is flagged as a free-surface, the flux of interfacial area getting out of it is replaced with the free-surface entrainment model. The green cell is a standard cell, the flux of interfacial area is unchanged.

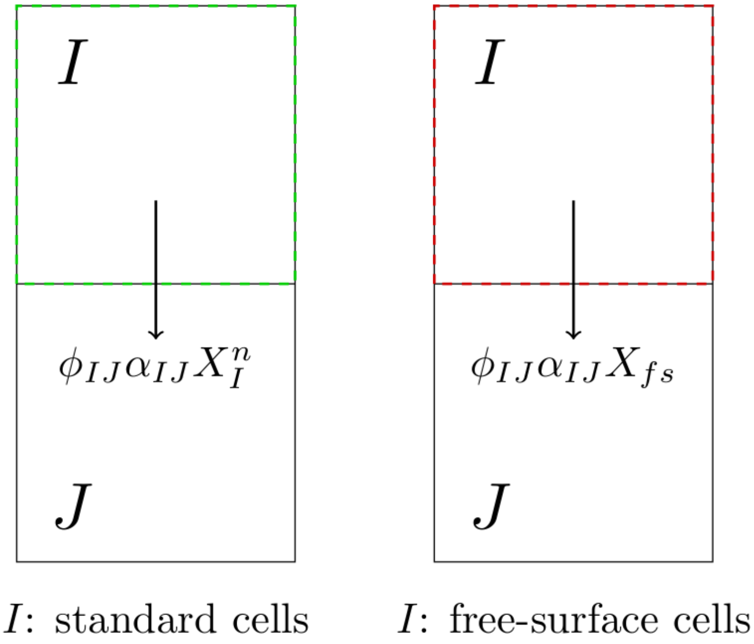

Figure 2: On the left, two standard cells; on the right, the cell above contains a large interface. The convective flux is supposed positive from cell I to cell J.

This concludes the presentation of the modifications to the interfacial area transport equations. Now, interfacial area transported out of a region containing a free-surface only depends on the model for X_{fs} effectively isolating the dispersed inclusions from the continuous air structures.

3.3 Model for the diameter of entrained bubbles

This section focuses on determining the expression of the free-surface source term X_{fs} in the interfacial area transport equation. This value characterises the size of air inclusions transported from the free-surface to the water region. To express this term, we have to make certain assumptions already hinted at in the introductory parts. Let us first assume that air entrainment is exclusively caused by the collisions between water turbulent eddies and the free-surface. This is likely to be the case in large scale coherent jets. Then, when created, an air structure located below the free-surface is subsequently broken up into smaller and smaller bubbles until turbulence is no longer intense enough to generate even smaller bubbles. This limit is known in the literature as the Hinze diameter d_h and can be expressed with an experimentally measured Weber critical number $W_{e,c}$, the fluid properties and the fluid turbulent quantities.

$$d_h = \left(\frac{W_{e,c}\sigma}{2\rho_w}\right)^{3/5} \epsilon_w^{-2/5} \tag{16}$$

Where σ is the surface tension coefficient between air and water and ϵ_w is the water turbulent kinetic energy dissipation. By further assuming this breakup process takes place near the free-surface and fast compared to the other fluid time scales, it is possible to use d_h for the expression of X_{fs}. It works as if a breakup cascade takes place near the surface and ends up with the creation of bubbles of diameter d_h. We do not model what is occurring during the cascade but only focus on its output.

Due to the nature of its definition, this term is independent on the mesh as long as the turbulence model remain consistent with mesh refining. Other models for the entrained air bubble diameter were discarded because of this. In practice critical Weber number values can be found in the literature and the typical range is $W_{e,c} \in [1,5]$ [29]. We will check its influence in the comparison with experimental data.

4. COMPARISON WITH EXPERIMENTAL DATA

In this section, we present a comparison between simulation results obtained with the air entrainment model and experimental data. Some details are also shown regarding the previous results obtained without models and the current new results. The experimental cases selected are meant to cover different range of entrainment regimes to show the applicability of the model in different conditions.

4.1 Over-flowing rectangular jet

This experimental setup consists in an overflowing nappe pouring into a water cushion [30]. It is considered to be a large scale air entraining configuration. Figure 3 sums up the geometrical aspects of the experimental device as well as the flow characteristics. $J_i = 0.085$ m^2/s is the inlet specific flux arriving in the upper tank, y_{C95} is the vertical coordinate where the air volume fraction reaches 95% in the lower reservoir, $H = 2.52$ m is the total height of the overflowing jet starting point and x_j is the position of the stagnation point where the fluid pressure is at its maximum along the bottom wall boundary.

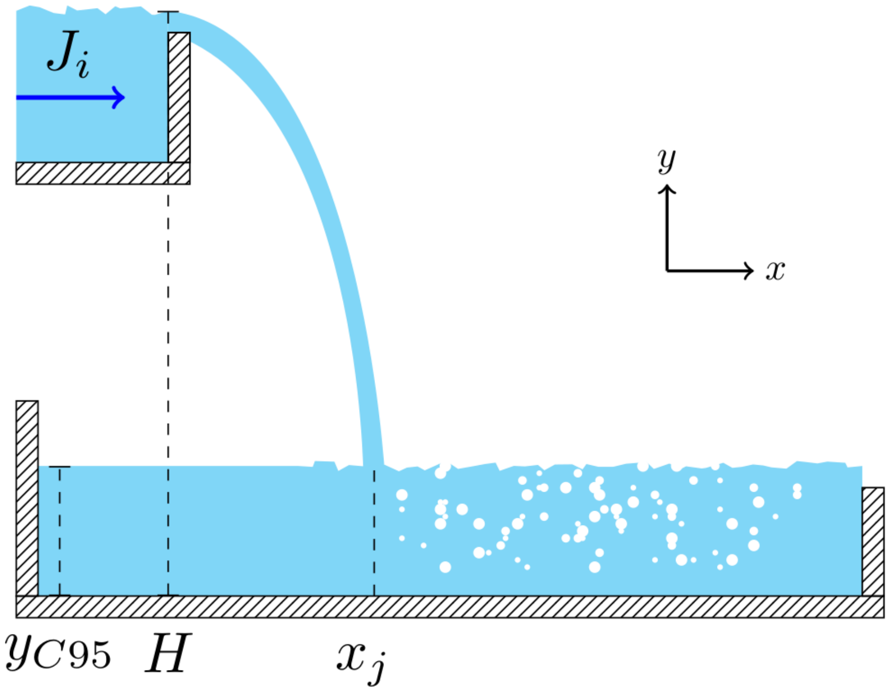

Figure 3: Experimental setup for the over-flowing jet.

The experimental data is obtained with the analysis of conductivity probes measurements on vertical profiles downstream the jet impact as well as macroscopic quantities such as the water cushion height and the stagnation point. The probes measurements include water axial velocity, air volume fraction and air bubble diameter.

The simulation is set up with a standard air-water mixture, turbulence is taken into account with a second order RSM model and polydispersion as well as the entrainment model are activated for dispersed air. Initially the upper tank and the water cushion are filled with water and more water is injected from the top left hand side inlet in the upper tank, causing the reservoir to overflow. Three 2D meshes have been studied which contain 300k, 700k and 1.5M cells respectively. Figure 4 shows the results obtained for water velocity and air volume fraction on different vertical profiles. The fine mesh gives sufficiently good results for a reasonable amount of computing time. We will keep it for further simulations. $u_{w,x}$ is the water velocity along the x-axis and α_g is the air volume fraction.

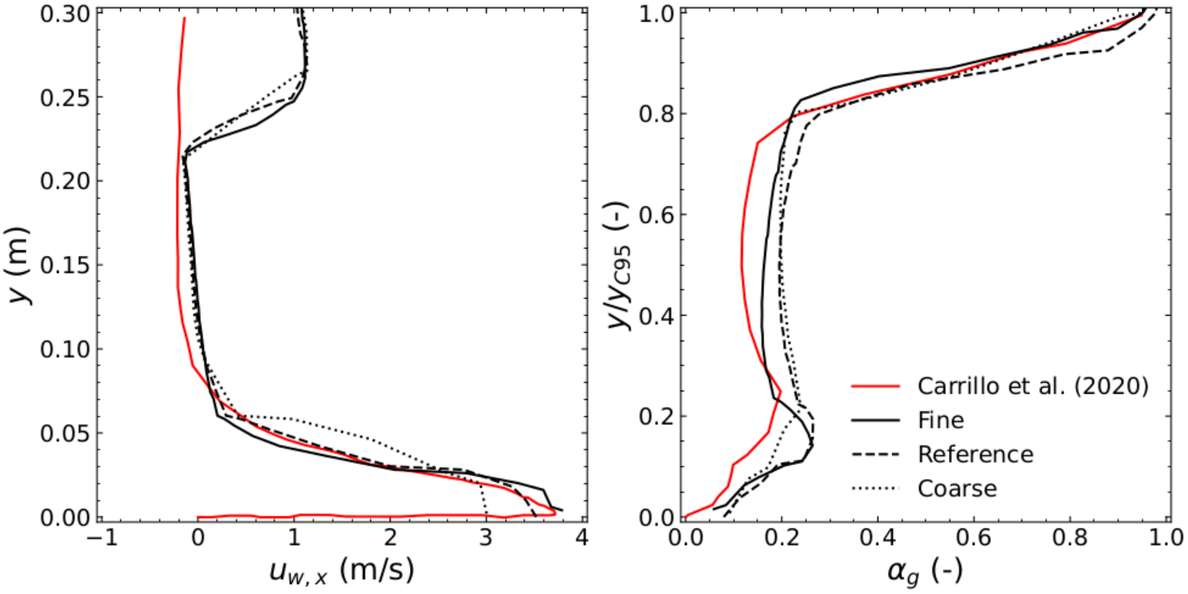

Figure 4: Mesh convergence study with $W_{e,c} = 5$.

Figure 4 also shows the correct prediction of fluid velocity near the wall. This seems to confirm that the turbulence model and the free-surface detection technique are appropriate for this case. In further results we do not present velocity plots and focus only on air volume fraction α_g and air bubble mean diameter d_b. Figure 5 compares the results obtained with the new model to those obtained with a specified diameter d_e for the entrainment process. As can be seen, results with the new model are at least as good as those obtained when the diameter is chosen beforehand. This is encouraging since the goal of the model is to avoid selecting a diameter which can be complicated in complex cases where no experimental data is available.

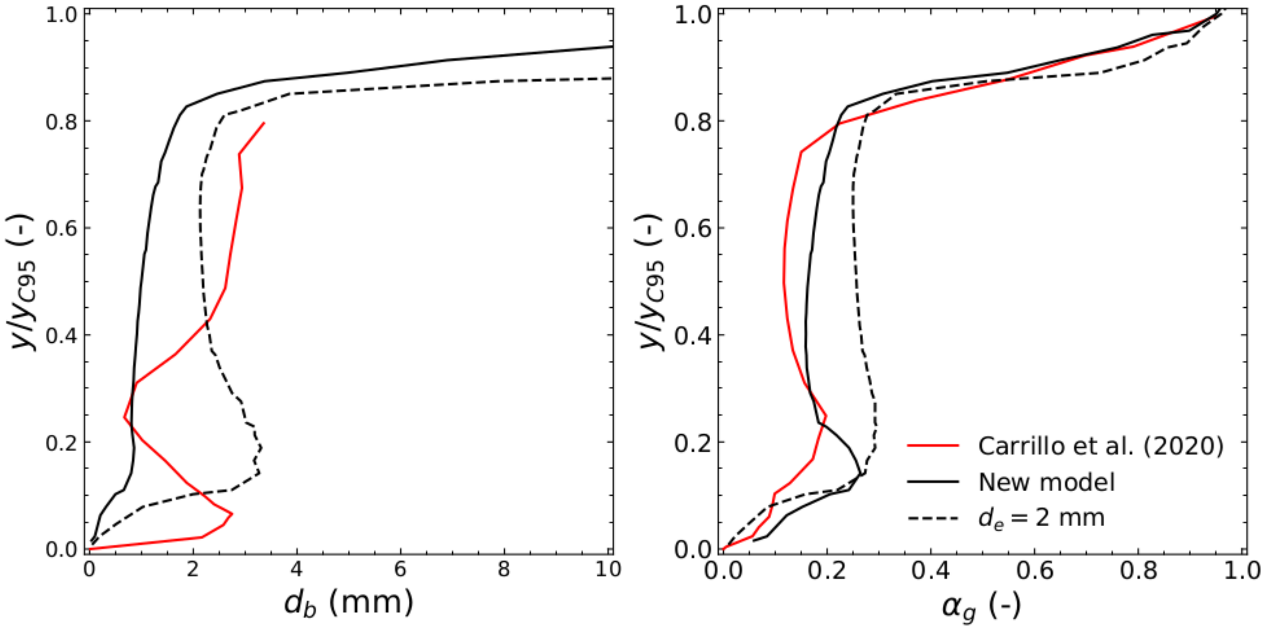

Figure 5: Comparison between results obtained with the new model with $W_{e,c} = 5$ (solid line) and those obtained when fixing the entrainment diameter $d_e = 2$ mm (dashed line).

Finally, we also plot the effect on the model of the critical Weber number $W_{e,c}$ in figure 6. Increasing the critical Weber number is equivalent to increasing the bubble diameter created by the entrainment process in our model. The results confirm this behaviour even though it is not as impactful as expected. Something to explore would be the fragmentation and coalescence model for the dispersed phase. For now, we have not investigated them in this case, but they may overestimate the breakup rate which would also affect our simulation results.

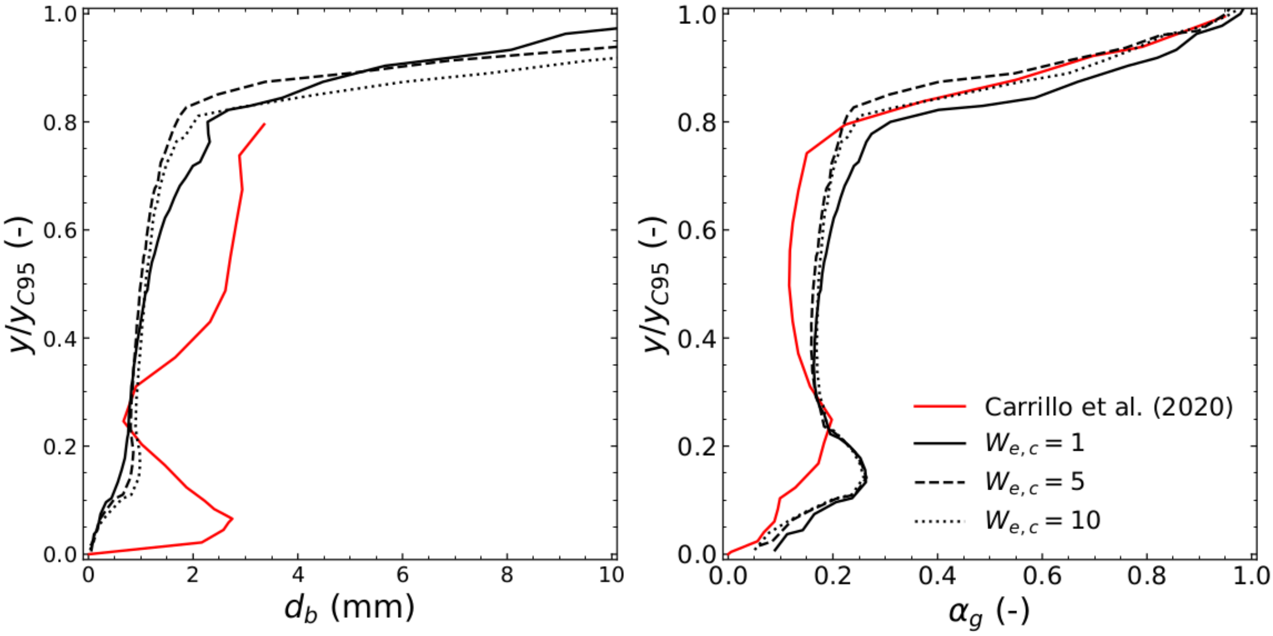

Figure 6: Study on the effect of changing the critical Weber number value.

All in all, we find the results on the bubble diameter prediction promising. They are not as close to the experimental results as we would like them, but the model still enables us to avoid fixing an arbitrary parameter upfront. Moreover, predicting a bigger bubble diameter would also reduce the quantity of air inside the lower reservoir thus enhancing the results on air volume fraction which are already consistent with experimental results.

4.2 Air entrainment in hydraulic jumps

This other case is quite different from the previous since it does not feature a jet. It consists in a critical free-surface stream (Froude number above 1) transitioning into a sub-critical stream (Froude number below 1). This configuration produces the widely known hydraulic jump phenomenon. From literature, it is clear that this process entrains air and the goal of this section is to assess the performance of the entrainment model for this type of flows. Figure 7 shows the geometric properties of the experimental setup [31] and the flow characteristics. The experimental measurements include void fraction and bubble diameter on vertical profiles downstream the hydraulic jump toe (at $x = x_j$). Comparison can also be made on global characteristics such as the hydraulic jump height. The comparison is made with other numerical results obtained with a VOF method and no entrainment model: the mesh is sufficiently fine to capture all relevant air structures [32] [33]. The experiments are classified according to the Froude numbers, the ratio between kinetic and potential energy $F_r = v/\sqrt{gL}$ where v is the fluid velocity, g is gravity and L is a characteristic length scale. In this section, we exclusively focus on the case $F_r = 2.43$ which corresponds to an inlet velocity $V_i = 1.64$ m/s.

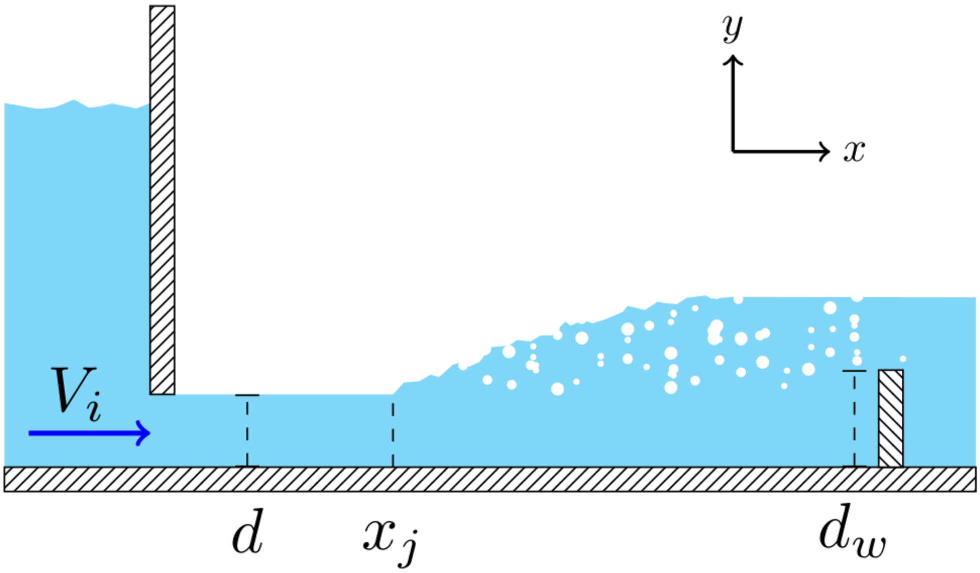

Figure 7: Geometric properties of the experimental setup. x_j locates the position of the jump.

The numerical simulation setup is illustrated in figure 8. The fluid is injected directly at $V_i = 1.64$ m/s and the obstacle of height $d_w = 0.89d$ downstream introduces the instability leading to the hydraulic jump. The 2D mesh contains around 300k Cartesian cells without a boundary layer refinement. The turbulence model is a second-order RSM model [34] and polydispersion as well as the entrainment model is taken into account for dispersed air. The volume is initially filled with air and water is injected from the bottom left inlet. When it impacts the obstacle at the end of the domain, the hydraulic jump forms and tends to move upstream until it starts oscillating around its equilibrium position.

Figure 8: Numerical setup of the hydraulic jump. Off plane boundaries are symmetries, on the bottom left-hand side is the inlet, red denotes a wall and green a pressure outlet.

Due to the unstable nature of the hydraulic jumps, we were unable to keep the toe of the jump from moving. In most simulations it oscillates around its equilibrium position. This is challenging since averaging tends to be affected by this behaviour. Therefore, a special averaging post-processing protocol had to be set up. It consists in averaging variables on profiles which are kept at a constant distance from the hydraulic jump effectively filtering its oscillation out.

The results obtained with neptune_cfd and the new air entrainment model are shown in figure 9. In these y_{C95} represents the vertical coordinate at which the air volume fraction reaches 95%, d_b is the bubble mean diameter and C is air concentration. The results are satisfying for void fractions as well as bubble diameters for various vertical profiles downstream the hydraulic jumps. The air bubble diameter prediction is especially noteworthy since it catches the increase near the free-surface illustrating its accuracy.

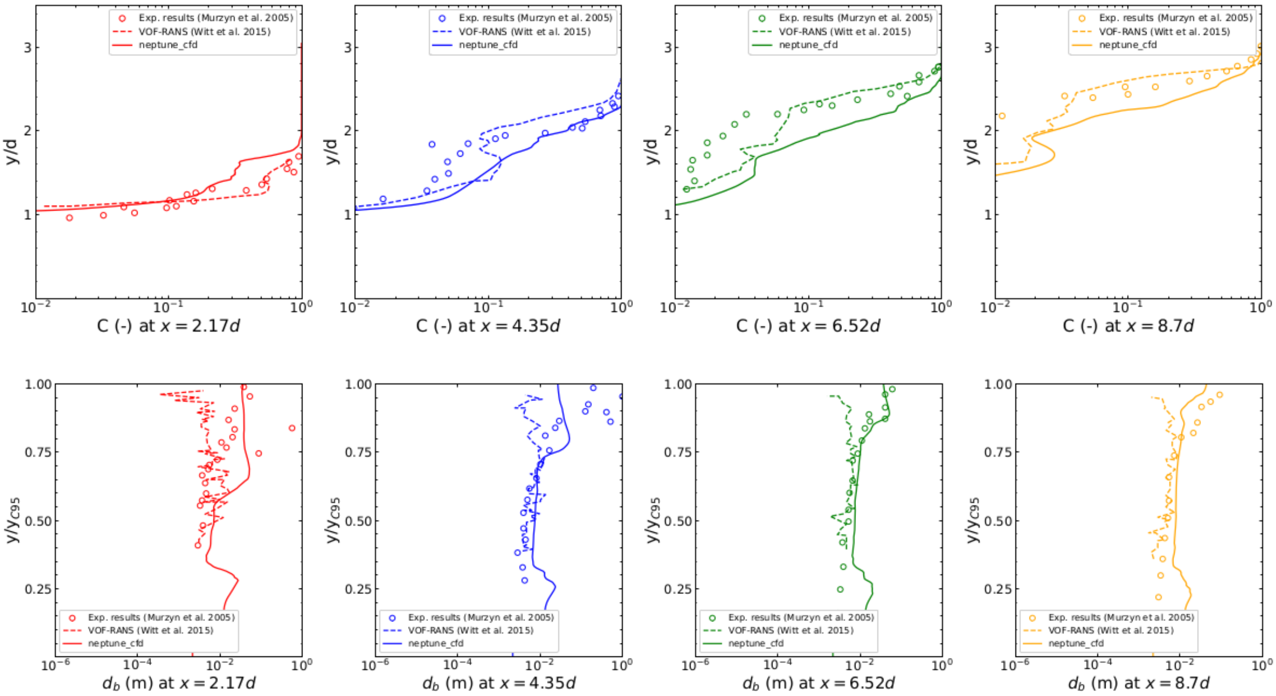

Figure 9: Comparison between experimental results and numerical results from the literature and results obtained with neptune_cfd

On the simulated air volume fraction profiles, it can be noted that too much air is entrained. This could be due to the incorrect bubble diameter prediction which seems not to be the case when we compare the predicted values with experimental data. Alternatively, it could be related to the air mass transfer from continuous structures to dispersed inclusions. Since it is an output of the model, we have very little leverage to act on it. It would require an overhaul of the twophase model. All in all, results are encouraging and show consistency in this complex case especially for the mean bubble diameter prediction d_b which is the core of the new model.

5. CONCLUSIONS

In this paper, we presented the multiphase solver neptune_cfd and the new modeling technique used to predict the diameter of bubbles created from an air entrainment mechanism. We have tested the model and compared it to experimental as well as numerical results on two different air entraining configurations: the rectangular jet and the hydraulic jump. The model shows great consistency in both cases and the reasonable impact of its parameter, the critical Weber number, has been highlighted. This shows the relevance of the model to tackle air entrainment phenomenon.

Looking ahead, we want to continue working on the numerical aspects of the model specifically to adapt coalescence and breakup terms to it. Turbulence may also be severely impacted by air entrainment. This impact should be studied in the future. Verifying its behaviour on other experimental configurations is also worth exploring.

ACKNOWLEDGEMENTS

The authors acknowledge having benefited from partial funding from ANRT under CIFRE contract 2020/1251.

REFERENCES AND CITATIONS

[1] M. Brocchini et D. H. Peregrine (2001), The dynamics of strong turbulence at free surfaces. Part 1. Description, *Journal of Fluid Mechanics,* **449**, 225-254.

[2] M. Brocchini et D. H. Peregrine (2001), The dynamics of strong turbulence at free surfaces. Part 2. Free-surface boundary conditions, *Journal of Fluid Mechanics,* **449**, 255-290.

[3] K. J. Sene (1988), Air entrainment by plunging jets, *Chemical engineering science,* **43**, 2615-2623.

[4] K. T. Kiger et J. H. Duncan (2011), Air-entrainment mechanisms in plunging jets and breaking waves, *Annual Review of Fluid Mechanics,* **44**, 563-596.

[5] N. Bertola, H. Wang et H. Chanson (2018), A physical study of air–water flow in planar plunging water jet with large inflow distance, *International Journal of Multiphase Flow,* **100**, 155-171.

[6] J. Belden, S. Ravela, T. T. Truscott et A. H. Techet (2012), Three-dimensional bubble field resolution using synthetic aperture imaging: Application to a plunging jet, *Experiments in Fluids,* **53**, 839-861.

[7] R. G. Ramirez de la Torre, M. Kuchta et A. Jensen (2020), Experiments on air entrainment produced by a circular free falling jet, *International Journal of Multiphase Flow,* **132**.

[8] L. Deike, W. K. Melville et S. Popinet (2016), Air entrainment and bubble statistics in breaking waves, *Journal of Fluid Mechanics,* **801**, 91-129.

[9] W. Mostert, S. Popinet et L. Deike (2022), High-resolution direct simulation of deep water breaking waves: Transition to turbulence, bubbles and droplets production, *Journal of Fluid Mechanics,* **942**.

[10] F. J. Moraga, P. M. Carrica, D. A. Drew et R. T. Lahey (2008), A sub-grid air entrainment model for breaking bow waves and naval surface ships, *Computers and Fluids,* **37**, 281-298.

[11] J. Ma, A. A. Oberai, D. A. Drew et R. T. Lahey (2012), A two-way coupled polydispersed two-fluid model for the simulation of air entrainment beneath a plunging liquid jet, *Journal of Fluids Engineering, Transactions of the ASME,* **134**.

[12] A. M. Castro, J. Li et P. M. Carrica (2016), A mechanistic model of bubble entrainment in turbulent free surface flows, *International Journal of Multiphase Flow,* **86**, 35-55.

[13] D. Valero et R. García-Bartual (2016), Calibration of an Air Entrainment Model for CFD Spillway Applications, *Springer Water,* 571-582.

[14] J. Ma, A. A. Oberai, D. A. Drew, R. T. Lahey et M. C. Hyman (2011), A comprehensive sub-grid air entrainment model for RaNS modeling of free-surface bubbly flows, *Journal of Computational Multiphase Flows,* **3**, 41-56.

[15] M. Xiang, S. C. Cheung, J. Y. Tu et W. H. Zhang (2014), A multi-fluid modelling approach for the air entrainment and internal bubbly flow region in hydraulic jumps, *Ocean Engineering,* **91**, 51-63.

[16] P. Lopes, G. Tabor, R. F. Carvalho et J. Leandro (2015), Modelling air-entrainment in circular, 3D plunging jet using the OpenFOAM CFD toolbox.

[17] M. Ishii et T. Hibiki (2011), Thermo-fluid dynamics of two-phase flow (Second edition), Springer New York.

[18] P. Coste (2013), A large interface model for two-phase CFD, *Nuclear Engineering and Design,* **255**, 38-50.

[19] O. Simonin (1996), Combustion and turbulence in two-phase flows, *lectures at the Von Karman Institute*.

[20] D. Z. Zhang et A. Prosperetti (1994), Averaged equations for inviscid two-phase flow, *Journal of Fluid Mechanics,* **267**, 185-219.

[21] J. Laviéville, N. Mérigoux, M. Guingo, C. Baudry et S. Mimouni (2017), A Generalized turbulent

dispersion model for bubbly flow numerical simulation in NEPTUNE_CFD, *Nuclear Engineering and Design*, **312**, 284-293.

[22] M. Ishii et N. Zuber (1979), Drag coefficient and relative velocity in bubbly, droplet or particulate flows, *AIChE*, 843-855.

[23] S. Mimouni, J. Laviéville, N. Seiler et P. Ruyer (2011), Combined evaluation of second order turbulence model and polydispersion model for two-phase boiling flow and application to fuel assembly analysis, *Nuclear Engineering Design*, 4523-4536.

[24] N. Zuber (1964), On the dispersed two-phase flow in the laminar flow regime, *Chemical Engineering Science*, 897-917.

[25] P. Coste et J. Laviéville (2015), A turbulence model for large interfaces in high Reynolds two-phase CFD, *Nuclear Engineering and Design*, **284**, 162-175.

[26] N. Mérigoux (2022), Multiphase Eulerian-Eulerian CFD supporting the nuclear safety demonstration, *Nuclear Engineering and Design*, **397**.

[27] P. Ruyer, N. Seiler, M. Beyer, F-P.Weiss (2007), A bubble size distribution model for the numerical simulation of bubbly flows, *proceedings of the 6th International Conference on Multiphase Flow*.

[28] M. J. Prince et H. W. Blanch (1990), Bubble Coalescence and Break-Up in Air-Sparged Bubble Columns, *AIChE*, **36**.

[29] F. Risso et J. Fabre (1998), Oscillations and breakup of a bubble immersed in a turbulent field, *Journal of Fluid Mechanics*, **372**, 323-355.

[30] J. M. Carrillo, L. G. Castillo, F. Marco et J. T. García (2020), Experimental and Numerical Analysis of Two-Phase Flows in Plunge Pools, *Journal of Hydraulic Engineering*, **146**.

[31] F. Murzyn, D. Mouaze et J. R. Chaplin (2005), Optical fibre probe measurements of bubbly flow in hydraulic jumps, *International Journal of Multiphase Flow*, **31**, 141-154.

[32] A. Witt, J. Gulliver et L. Shen (2015), Simulating air entrainment and vortex dynamics in a hydraulic jump, *International Journal of Multiphase Flow*, **72**, 165-180.

[33] A. Witt, J. S. Gulliver et L. Shen (2018), Numerical investigation of vorticity and bubble clustering in an air entraining hydraulic jump, *Computers and Fluids*, **172**, 162-180.

[34] C.G. Speziale, S.S. Sarkar et T.B. Gatski (1991), Modelling the pressure-strain correlation of turbulence: an invariant dynamical systems approach, *Journal of Fluid Mechanics*, **227**, 245-272.